Can Wang, An Deng, Abbas Taheri

Three-dimensional discrete element modeling of direct shear test for granular rubber-sand

Computers and Geotechnics, 2018; 97:204-216

Final publication at http://dx.doi.org/10.1016/j.compgeo.2018.01.014

Three-dimensional discrete element modeling of direct shear test for granular rubber–sand

Can Wang, An Deng*, Abbas Taheri

School of Civil, Environmental and Mining Engineering, The University of Adelaide, SA 5005, Australia.

* Corresponding author.

E-mail addresses: c.wang@adelaide.edu.au (Can Wang). an.deng@adelaide.edu.au (An Deng). abbas.taheri@adelaide.edu.au (Abbas Taheri).

ABSTRACT

Three-dimensional discrete element modeling of direct shear test conducted on granular rubber–sand is presented. Excellent agreement was attained between the simulation and test results, verifying the model's capacity of examining mixtures shear behavior. Important particulate-scale observations were attained, including the inter-particle contacts force, particles displacement and rotation, porosity and their variation with rubber particle contents. The observations demonstrate that the rubber particles inclusion amends the mixture stiffness, grading and packing at the particulate level, leading to a corresponding variation in the material shear behavior. Some interesting particulate-level simulations were examined to gain further insight into micro-mechanic characteristics of the mixtures.

Keywords: direct shear test; rubber; sand; discrete element; contact force; shear band.

INTRODUCTION

There are approximately 48 million tons of waste tires per year generated in Australia; a low percentage is recycled or managed properly [1]. An important solution to increasing the recycling rate is to process the wheels tire into a range of smaller pieces of rubber (e.g., shreds, chips, particles or fine powers) and incorporate the sliced rubber elements as reinforcements into soils [2-4]. The formed mixtures outperform the soils in respect to resilience, strength, ductility and damping [5-7]. The demonstrated advantages arises from the rubber material's capacity of increasing inter-particle interactions which were confirmed in triaxial [3, 5, 8-9], direct shear [10-13] and uniaxial pull-out tests [14].

Rubber particles can be mixed with sand into rubber–sand fill [11]. The fill exhibits better workability than the shred- or chip-based mixtures [15]. For the same reason the granular rubber–sand mixtures avoid segregation problems and aim at applications where otherwise are difficult to access. Additional value lies in the rubber–sand being lighter in weight by 20–40% than the sand backfill depending on the materials per cent used [16]. The use of the lightweight material reduces loads acting on the surrounding infrastructures or utilities (e.g., retaining walls or pipelines). Rubber–sand is also graded to facilitate water percolation and drainage and thus avoid environment or climate related concerns such as frost heave. Direct shear tests conducted on rubber–sand samples suggested that the material shear strength remains similar in magnitude to that of sand, demonstrating a substitute for sand backfills [3, 16-17]. To understand the shear behavior, discrete element modeling was conducted on rubber–sand mixtures subjected to direct shear tests [3, 8, 12, 18-19]. These studies gained insight into the inter-particle interactions and demonstrated the role of rubber particles in changing the material fabrics and the material stiffness. Most of the discrete element simulations were implemented in a two-dimensional plane which under-represents the three-dimensional shape of the particles and neglects the boundaries associated with the samples [20-22]. The purpose of this study is to conduct three-dimensional numerical simulations on the rubber–sand subjected to direct shear tests. The discrete element method is used to conduct the simulations. The simulations are validated against laboratory test results and then deployed to examine how the rubber particles inclusion influences the material shear behavior.

MATERIALS AND METHOD

The materials include sand and rubber particles. The respective gradation curves are shown in Figure 1. The sand (D_{50}=0.58 mm) is well graded to fit into the pore space of the rubber particles (D_{50}=5 mm). Define specific volume fraction χ = the rubber particle specific volume over the total specific volume of the mixture. Design a series of samples with χ=0, 0.19, 0.34, 0.47, 0.58 and 1, respectively, where χ=0 and χ=1 define the pure sand and the pure rubber particle samples, respectively. A mixture with χ>0.6 was not viable due to particles segregation [15, 23]. The corresponding weight fraction is 0, 0.1, 0.2, 0.3, 0.4 and 1, respectively. A mixer was used, following the steps shown in Ghazavi [11], to gain a uniformly distributed mixture.

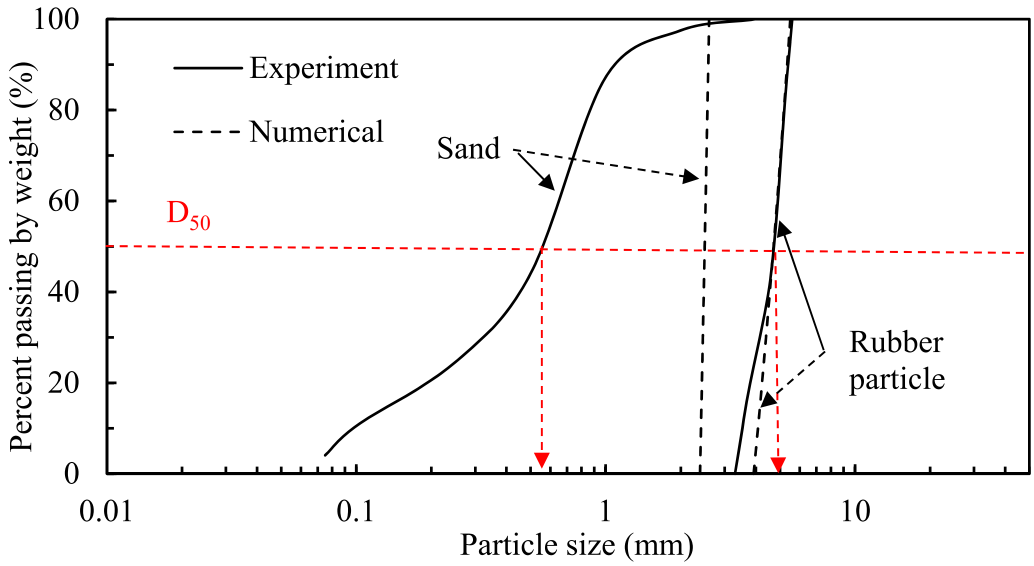

Figure 1 Particle size distribution of sand and rubber particles.

Standard direct shear tests were performed. The sample size measures 60*W*×60*L*×40*D* mm, which was chosen to satisfy the sample size vs. particle size criterion. Pour the sample into the shear boxes, and even and level the materials, enabling a uniform distribution. Prepare four identical samples for one fraction χ and subject the four samples to vertical load σ_v=100, 200, 300 and 400 kPa, respectively. Shear the samples at a rate of 1 mm/minute until the occurrence of the greatest shear stress or 5 mm displacement, whichever occurs earlier.

Discrete element simulation was conducted using a commercially accessible software package Particle Flow Code (PFC) 3D. Assemble together ten pieces of wall (a PFC simulation object) to form a compartment, with respective dimensions representing the shear boxes, as shown in Figure 2. Inside the box compartment is the spherical particles assembly, with the particle sizes designed in agreement with main portions of rubber particles and sands, respectively. A mass scaling [19] was applied to the particle sizes, enabling a better computer simulation, as having been attained in other studies [8, 24]. The scaling results are provided in Figure 1. Depending on the mixture examined, there are about 6,000 sand particles and 1,000 rubber particles created to fill up the boxes space. The mixture in the shear boxes is shown in Figure 2. After placing the particles inside the shear boxes, apply the servo-control method [25] to release excess sphere contact forces where there were.

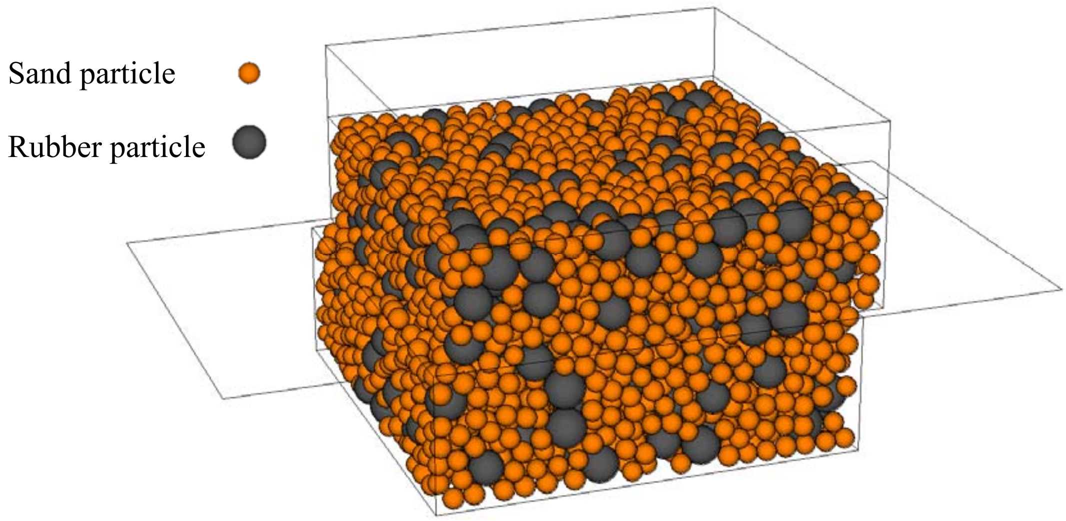

Figure 2 Material assembly in direct shear boxes.

The linear elastic model of PFC3D was used to replicate the shear stress–displacement relations. The linear model outperforms the nonlinear Hertz model in respect to the use of the servo-control, which is a model in-built developed to maintain a load acting onto the material [25]. The linear model is illustrated in Figure 3. Two entities (or particles), 1 and 2, interact. The interaction is modeled through a set of physical units: springs, dashpots and a slider. The springs are used to create a linear elastic relation between relative displacement and contact force. The dashpots are applied to provide viscosity at shear and normal directions, respectively. The material properties for the simulation are summarized in Table 1. In the table, the inter-particle properties were determined by PFC3D using the following equations:

$$\frac{1}{\boldsymbol{k}_{\boldsymbol{n}}} = \frac{1}{\boldsymbol{k}_{\boldsymbol{n},1}} + \frac{1}{\boldsymbol{k}_{\boldsymbol{n},2}} \tag{1}$$

$$\frac{1}{\boldsymbol{k}_{\boldsymbol{s}}} = \frac{1}{\boldsymbol{k}_{\boldsymbol{s},1}} + \frac{1}{\boldsymbol{k}_{\boldsymbol{s},2}} \tag{2}$$

$$\mu = \min(\mu_1, \mu_2) \tag{3}$$

where k_n and k_s are normal and shear stiffness at contact; $k_{n,1}$ and $k_{n,2}$ are normal stiffness of entity 1 and 2, respectively; $k_{s,1}$ and $k_{s,2}$ are respective shear stiffness; μ is inter-particle friction coefficient; μ_1 and μ_2 are respective entity surface friction.

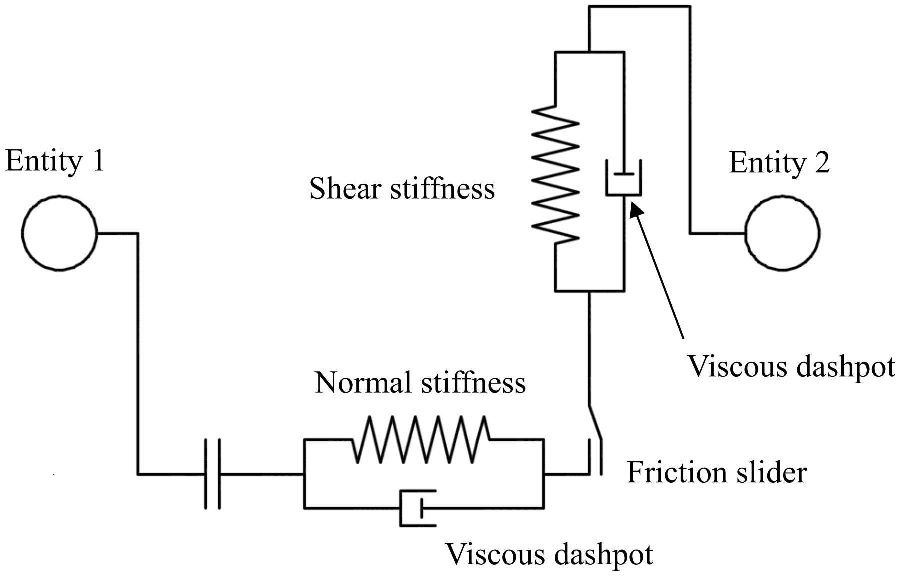

Figure 3 Inter-particle linear contact model.

Table 1 Micro- properties for discrete element simulation.

Property	Value		
	Sand particle	Rubber particle	Shear box
Contact normal stiffness, k_n (N/m)	5.9×10^7	8×10^5	1×10^8
Contact shear stiffness, k_s (N/m)	5.9×10^7	8×10^5	1×10^8
Particle diameter, d (mm)	2.4–2.6	4–5.5	N/A
Specific density of solid, G_s	2.65	1.2	N/A
Damping coefficient, ζ	0.7	0.7	N/A
Inter-particle friction coefficient, μ	0.55	0.60	0.20

As suggested in previous studies [26-28], the quartz sand stiffness falls into the order of magnitude of $\times10^7$ N/m. A lower order of magnitude of $\times10^5$ N/m was suggested for rubber material [29]. These values were taken as the points to depart and, as suggested in Coetzee and Els [30], plugged into numerical iterations of harmonizing the shear test results, aiming at obtaining the final stiffness and other micro-properties. The simulations are shown in Figure 4. Excellent agreement is obtained between the test and simulation results for all series of tests. That means the material properties in Table 1 are verified as input values for the discrete element model to replicate the particles motion. All of the samples exhibit a strain-hardening relation where there is no clear occurrence of failure. The relationship agrees with the results provided in similar rubber–sand studies (e.g., [10]). The strain-hardening relationships become pronounced when the applied vertical load σ_v or rubber content χ increases. The strain-hardening curves suggest two aspects: *i*) the sand samples are loosely packed when sheared and there is no clear shear dilation; and *ii*) the rubber particles inclusion improves the material packing. The improved packing promotes the material strain-hardening characteristics as well as ductility, which is in favor of stability of backfilling works.

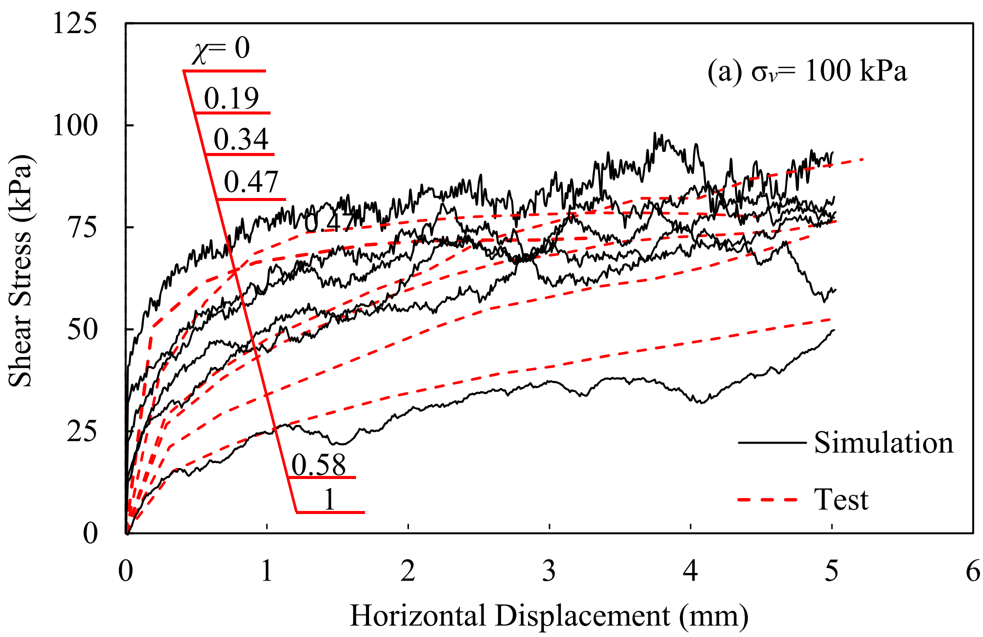

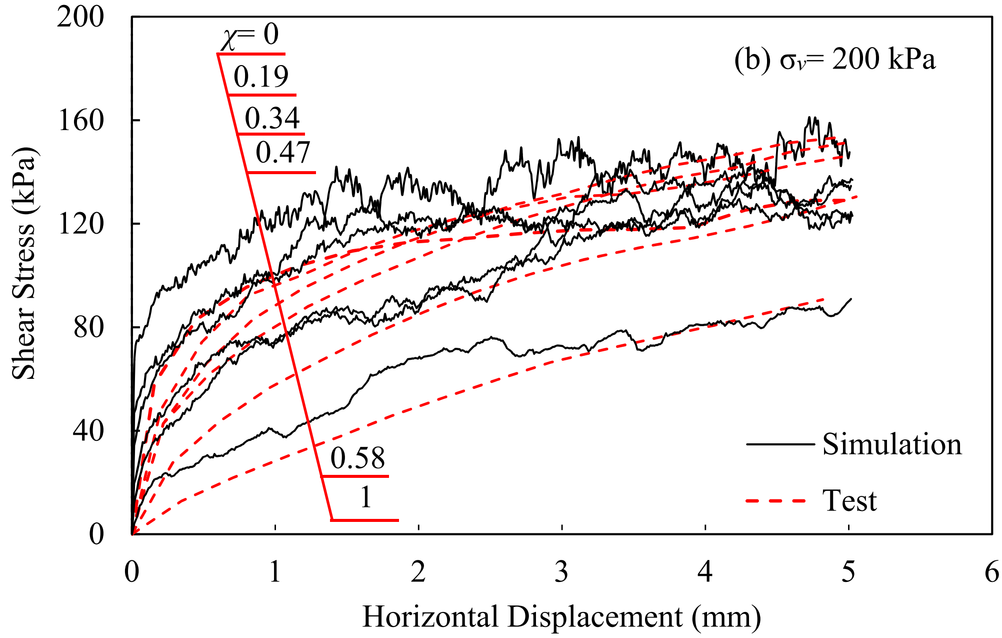

(b) σv= 200 kPa
χ= 0
0.19
0.34
0.47
0.58
1
Simulation
Test
Shear Stress (kPa)
Horizontal Displacement (mm)
0
40
80
120
160
200
0
1
2
3
4
5
6

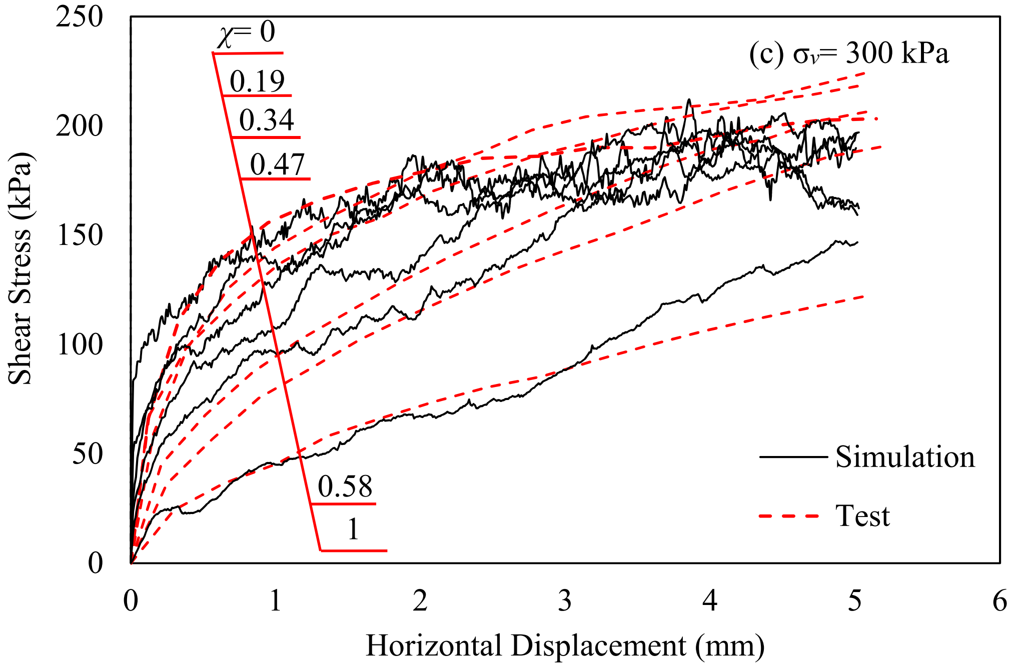

(c) σv= 300 kPa
χ= 0
0.19
0.34
0.47
0.58
1
Simulation
Test
Shear Stress (kPa)
Horizontal Displacement (mm)
0
50
100
150
200
250
0
1
2
3
4
5
6

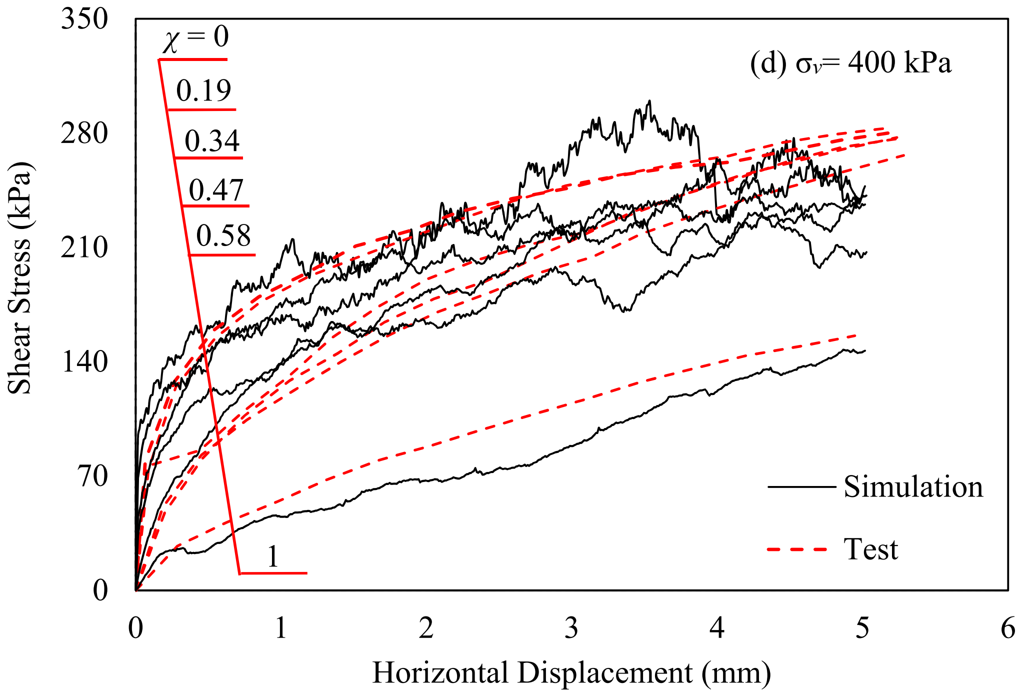

Figure 4 Shear stress–displacement curves for samples subjected to direct shear test with varying vertical loads.

PARTICULATE-SCALE SIMULATION RESULTS

Packing

The material packing is illustrated in Figure 5. Four assemblies are presented: rubber particles, loose-packing rubber–sand, dense-packing rubber–sand, and sand. The assemblies vary in mix fraction, leading to material porosity variation. The rubber particles assembly (i.e., the leftmost diagram) exhibits the greatest porosity. The porosity decreases with the sands inclusion, as the sand particles are finer enough to sit in the pore space formed by the rubber particles skeleton, i.e., the two middle diagrams. The trend, however, seems not to continue into the sand assembly; the sand assembly does not yield the least porosity. Plot one single presumed rubber particle in red in the sand assembly as shown in the rightmost diagram. The presumed rubber particle works better to reduce the pore space than the lot of the equivalent sand particles does. That is, there is a rubber fraction enabling packing optimization. To work out the optimal fraction, a set of eleven assemblies of different mix fractions is packed through simulations, aiming at developing the porosity vs. mix fraction relationship. The relationship is shown in Figure 6 (i.e., the primary axis vs. the horizontal axis). It is shown that the porosity vs. rubber fraction relationship is not monotonic but concave. The transition sits on sample χ=0.6, less than which the porosity decreases with χ; otherwise the opposite. Therefore χ=0.6 is identified as the optimal packing mix. Similar packing characteristics occur to other binary mixtures. Kim and Santamarina [23] examined packing of sand and rubber chips (D_{50}=3.5 mm) mixtures and recommended an optimal packing fraction of χ=0.67. Mota *et al.* [31] assessed spherical glass beads (0.3 mm to 3.4 mm sizes) with 2 to 10 size ratios and confirmed a similar optimal fraction χ=0.6 to 0.7 for all series mixtures. All of these results suggest that packing is sensitive to particles size.

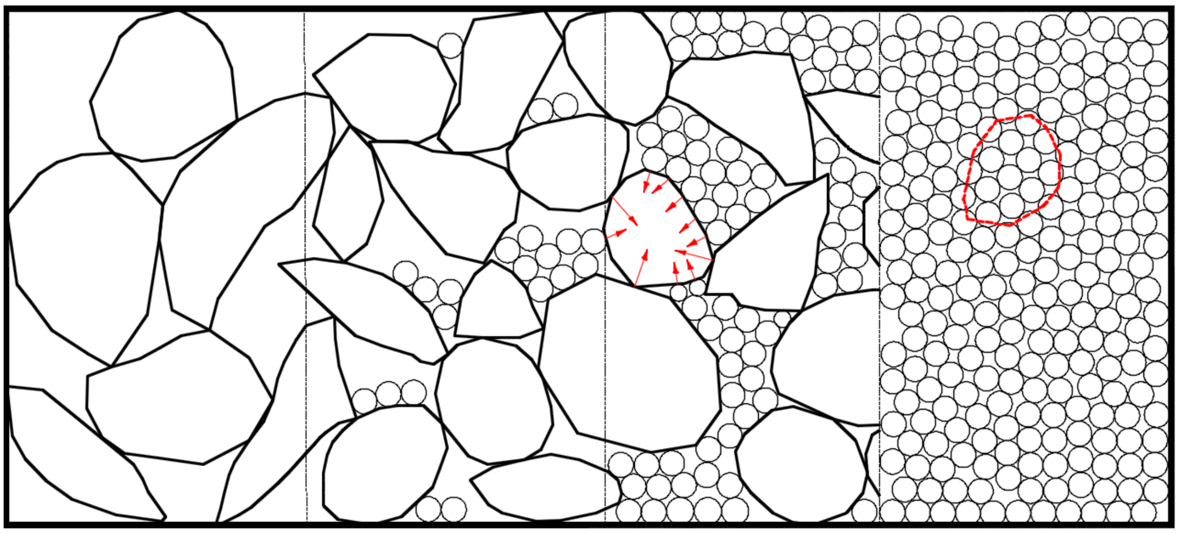

Rubber particles | Rubber-sand (loose-packing) | Rubber-sand (dense-packing) | Sand particles

Figure 5 Schematic of mixtures packing.

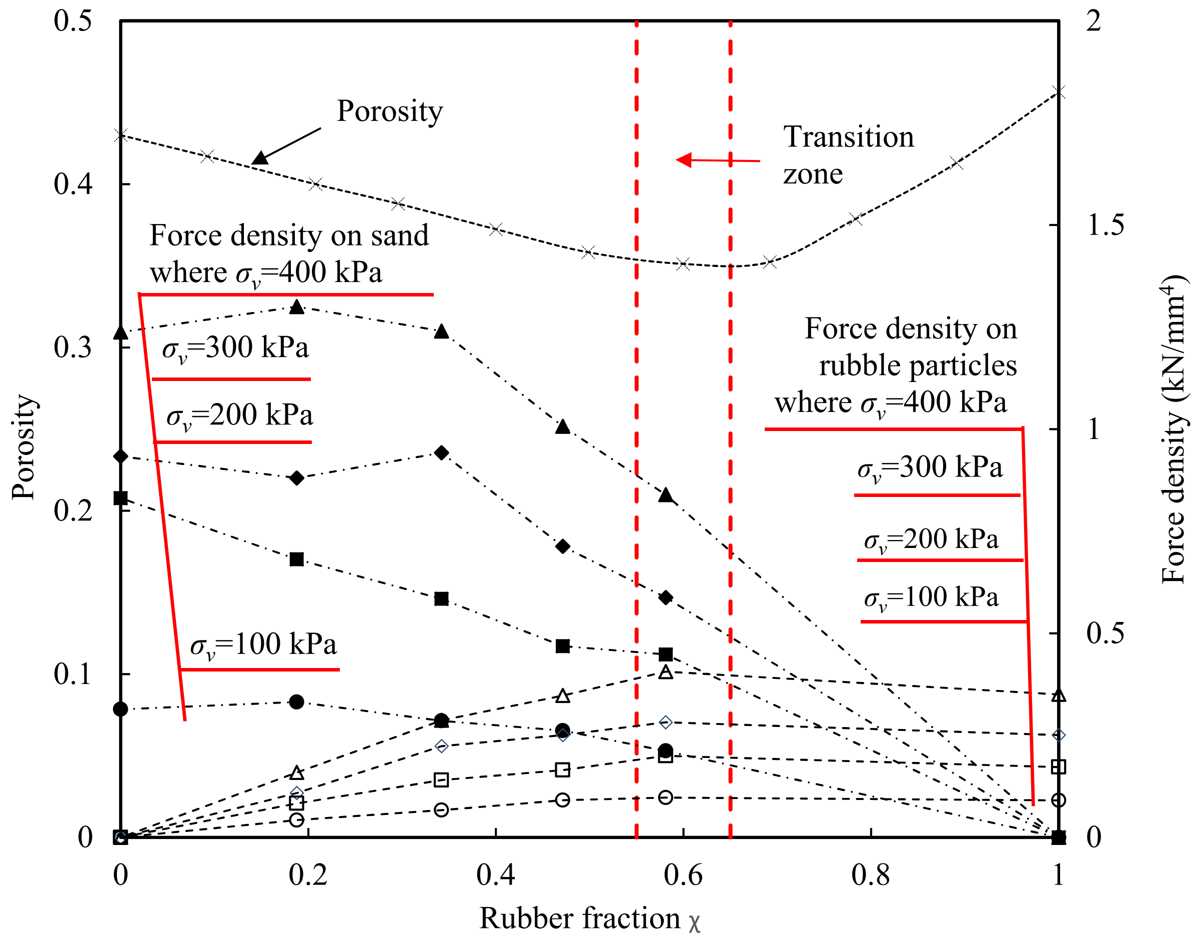

Figure 6 Porosity and force density for samples in direct shear simulations of varying vertical loads.

Additional mixtures of varying grading characteristics were examined. The simulation results are shown in Figure 7. Five mixtures are simulated, with a ratio of larger particle size, *D*, to smaller particle size, *d*, ranging from 10 to 2. An additional variant is the large particle fraction, χ_D, from 0 to 1, aiming at broadening the grading characteristics. The results suggest that the grading does influence the packing (i.e. porosity). The mixture becomes dense with *D*/*d* increase, meaning small particles infilling the pores of large particles. The infilling effect is optimal at $\chi_D \cong 0.6$, consistently across all of the five series of mixtures. This optimal value agrees with those test results provided in Mota *et al.* [31].

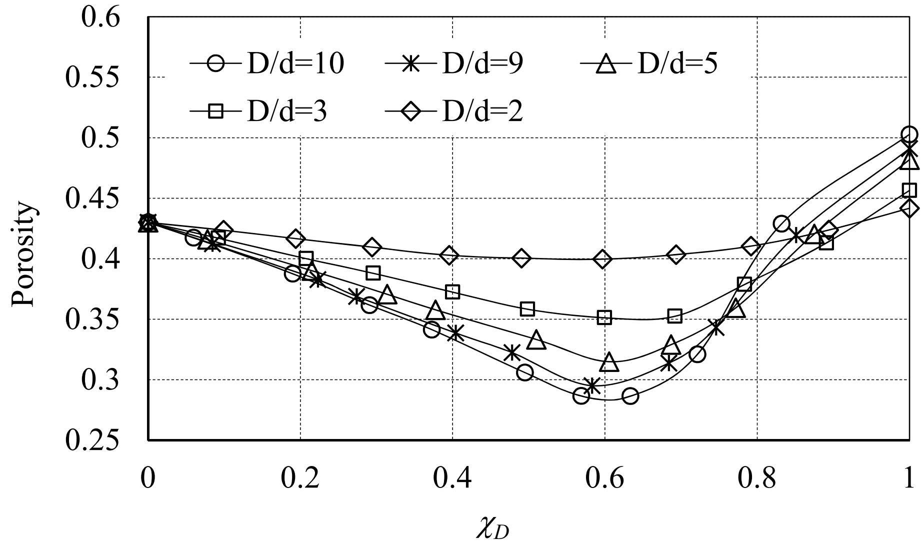

Figure 7 Porosity changes due to varying mixture fraction and particle size.

The secondary vertical axis of Figure 6 reads the force density for the samples examined. The force density is defined as the sum-of-force at contact, F, normalized to the sample volume, V, and mixture median diameter, D_{50}, i.e., F/(V×D_{50}). For demonstration purpose, the forces at the contacts of a single particle are illustrated in the third diagram in Figure 5. The value of F is the sum of the forces at the contacts of interest, e.g., the rubber particle contacts. Where a particular portion of particles is examined, the force density measures the particles capacity of sharing the inter-particle force. Figure 6 shows the force density at rubber (and sand) contact vs. rubber fraction curves, each corresponding to one of the four vertical loads (i.e., 100, 200, 300 and 400 kPa). For each of the curves, the rubble content is the only variant, with the rest conditions remain the same. The purpose is to examine the rubber (or sand) contact force with respect to rubber content where the load is constant. All of the four curves are convex; and the transitions occur consistently at χ = 0.58, at least for the rubber fractions examined. The transition points also agree with the optimal value χ = 0.6 for packing. Define a transition zone χ=0.55 to 0.65 where the assembly works best in packing and load sharing: the rubber fraction develops into a skeleton where the sands largely infill the skeleton pore spaces and enable optimal packing; in the meantime the rubber particles share the most significant portion of the loads and guarantee material strength capacity.

Inter-Particle Forces

The inter-particle forces are examined on sample χ=0.34 being sheared under the vertical load σ_v=200 kPa as an example. To gauge the forces evolution, select five points of *A* to *E* on the corresponding shear stress–displacement curve (Figure 8). The five points read displacement values of δ=0, 1, 4, 5 and 6 mm, respectively, aiming to span the complete shear process. In addition a separate shear is simulated which conducts an unloading-reloading process in the middle of shear, examining the damping behavior of the model. In the process, the boxes reverse from δ=2 mm to δ=1 mm, then are re-sheared to δ=6 mm. The unloading-reloading process creates a hysteresis loop, demonstrating the elastic-plastic behavior of the shear process. The unloading clearly and quickly releases the shear stress acting on the sample, and meanwhile an opposite shear force occurs and grows. Upon re-loading, the curve moves back to the point where unloaded, recovering the original shear stress released, and interestingly continues in a new pathway. The new pathway rises above that without the load loop, meaning the material stiffens. That is, the load loop helps compact the mixture and the damping properties assigned to the model reflects the physical behavior of the sample.

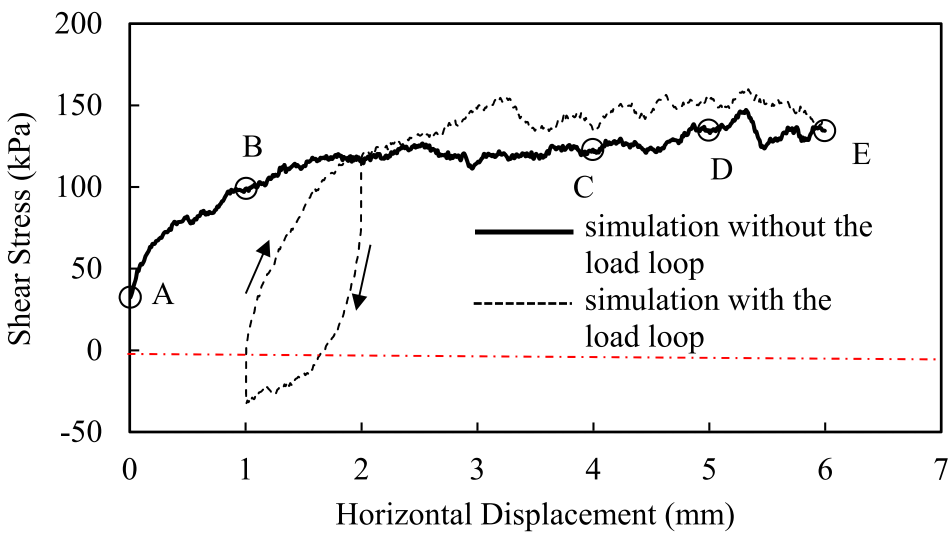

Figure 8 Shear stress vs. displacement curve for sample χ=0.34 sheared under σ_v=200 kPa.

The inter-particle forces are plotted as solid lines with its thickness proportional to the force magnitude [25]. The lines connect up into a chain between particles, forming a force chain. The corresponding normal contact force chains that are captured from the front view, together with the illustrated shear boxes, are shown in Figure 9. The normal contact force, in relation to the shear force, gives a better picture of the particles overlap and motion. The force chains for the sand sample (χ =0) sheared to δ=6 mm is also provided for comparison. It is clear that the contact forces progressively redistribute with the shear advance. The forces distribute evenly where there is no shear but the vertical load σ_v applied (Figure 9(a)). When the lower box advances to the left, a force concentration band evolves diagonally and becomes pronounced as shown in Figure 9(b–e), meaning greater normal contact forces oriented diagonally. When the shear advances, the force band becomes more diagonally oriented. Define a shear advance convention: it is a clockwise shear if the lower box displaces to the left, otherwise an anti-clockwise shear. The clockwise shear which is the case of Figure 9 leads to a force band oriented from the top–left corners to the bottom–right. It is plausible to infer that a top–right to bottom–left force band evolves if the shear acts anti-clockwise. Where sheared to the same displacement δ=6 mm, the sand sample (Figure 9(f)) exhibits similar force band orientation, but finer force chains than the corresponding rubber–sand sample does (Figure 9(e)). This suggests the capacity of rubber materials in concentrating the contact forces. The rubber particles inclusion brings forth to the soil matrix two changes: particles stiffness reduction and particle size increase. Both contribute to the contact forces concentration in view of contact mechanics. The contributions can be illustrated in Figure 10. An assembly of discs is enclosed in a box. The line between two contacting discs represents a contact force where the line thickness is proportional to the force magnitude. In Figure 10(a), the presumed larger disc is equivalent in area to the six smaller discs. The substitute shown in Figure 10(b) eliminates the inter-particle contacts bounded by the larger disc, reducing the total number of contacts in the assembly and therefore the number of force chains. In addition the material stiffness also alters the force chain. Where the assemblies are compressed as shown in Figure 10(c–d), a larger overlap at contact is captured by the software as a greater contact force. In the meantime, the void around large particle surface provides room for the neighboring small discs to rearrange. The rearrangement helps release a portion of the force developed between the small discs.

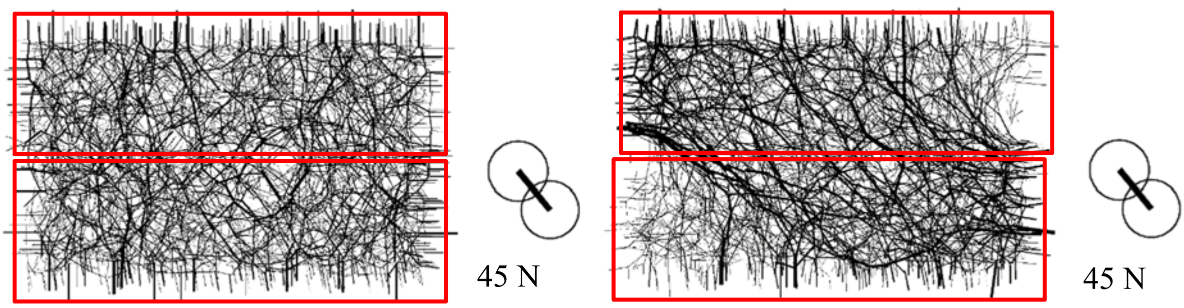

(a) δ=0 mm and χ =0.34 (b) δ=1 mm and χ =0.34

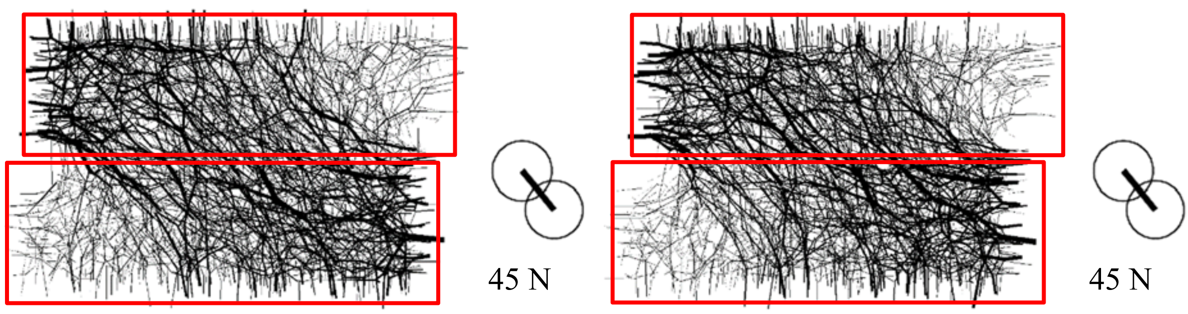

(c) δ=4 mm and χ =0.34 (d) δ=5 mm and χ =0.34

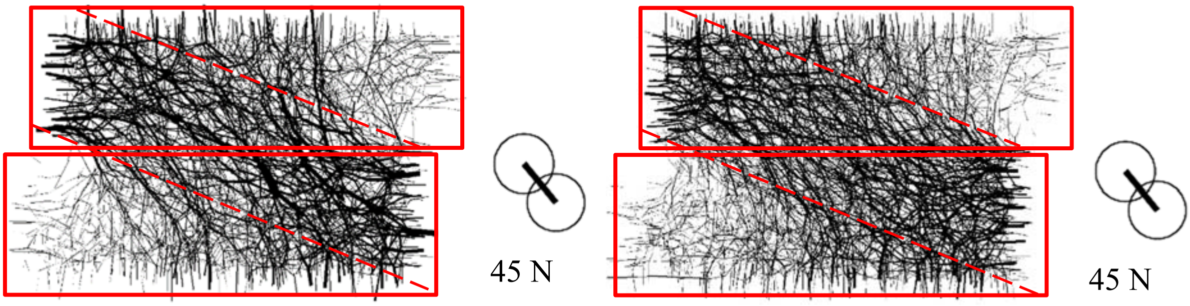

(e) δ=6 mm and χ =0.34 (f) δ=0 mm and χ =0

Figure 9 Contact force chains drawn at the same scale for samples sheared under σ_v=200 kPa to different distances.

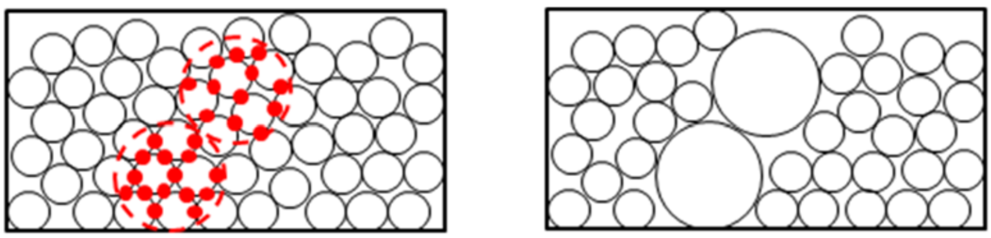

(a) Free-loading small discs assembly (b) Free-loading mixed discs assembly

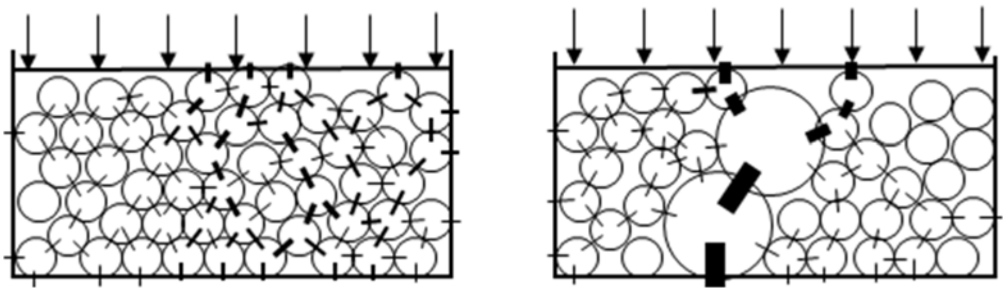

(c) Loaded small discs assembly (d) Loaded mixed discs assembly

Figure 10 Schematic of disc contacts under different load conditions.

The contact force is represented by plotting stress contour lines, aiming at mapping the stress and refining the force band orientation. The measurement sphere approach [25] is used to plot the stress contours. The sphere is designed to capture the equivalent stress field bounded by the sphere. Figure 11(a) illustrates the enlarged view of one measurement sphere as well as the influenced particles. Figure 11 (b) shows the measurement spheres designed to the shear boxes. A grid of 4×6 measurement spheres is created in the shear boxes. All of the spheres are equal in size with a diameter of 10 mm, occupying the inner space of the box. Each of the spheres is at least two times larger in size than the particles examined in the direct shear test and can accommodate up to twenty particles depending on the particles size.

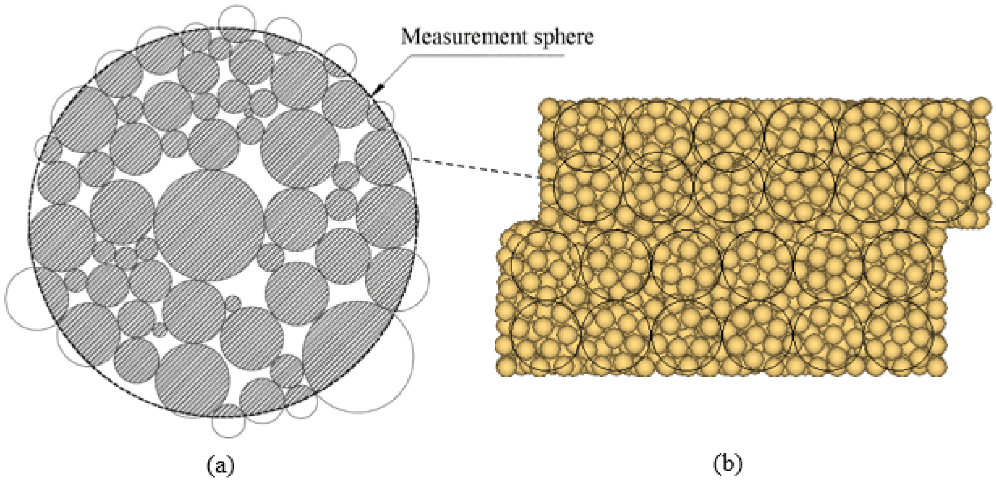

Figure 11 Diagram of measurement sphere approach: (a) one measurement sphere and bounded particles, and (b) a grid of measurement spheres designed in the shear box.

The stress contour maps plotted for the sand sample before and after the shear test are shown in Figure 12. The shear as an example is conducted under the vertical load σ_v=200 kPa until the displacement δ=6 mm. Plot the contours at three separate vertical planes: the front, middle and back, enabling a 3D view of the stress distribution. The set of contour lines is plotted by using the software package MATLAB to process the stress values captured by the measurement spheres. In a measurement sphere, the stress value is defined as the mean stress at contact, σ_m, which is expressed as $\sigma_m=(\sigma_{xx}+\sigma_{yy}+\sigma_{zz})/3$ where the dimensional stress σ_{xx}, σ_{yy} and σ_{zz} are provided by PFC 3D. It is noteworthy that the contour lines draw on the centers of measurement spheres; therefore the margins are not mapped. The stress contours in Figure 12(a, c and e) show that the samples remain broadly even in contact stress before the shearing. At a few spots (e.g. the bottoms and corners) the stress values are relatively lower due to the arching created as illustrated in the broken curves. The overall stress values on the map agree with the vertical load σ_v =200 kPa. Where sheared, the sample develops new contour maps as shown in Figure 12(b, d and f). The changes include the contours orientation to the diagonal, stress concentrations in the upper–left and lower–right corners, and uneven stress distribution on the shear plane. These changes confirm the past research outcomes [32-33] that displacement (and shear stress) is not constant on the shear plane and the active and passive pressure zones evolve in the lower and upper boxes, respectively.

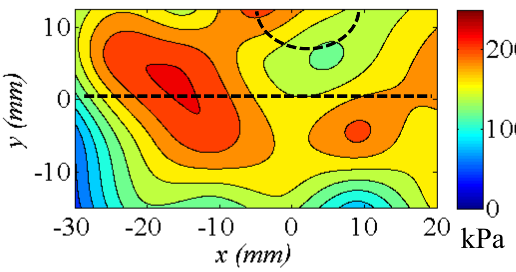

(a) δ=0 mm (front plane)

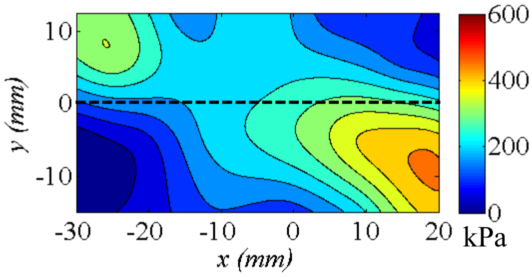

(b) δ=6 mm (front plane)

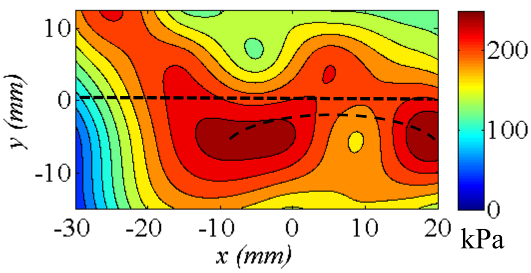

(c) δ=0 mm (middle plane)

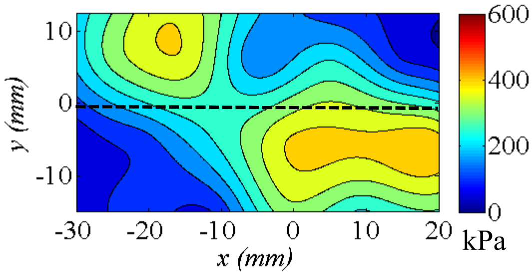

(d) δ=6 mm (middle plane)

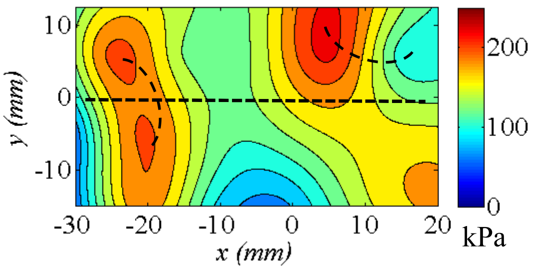

(e) δ=0 mm (back plane)

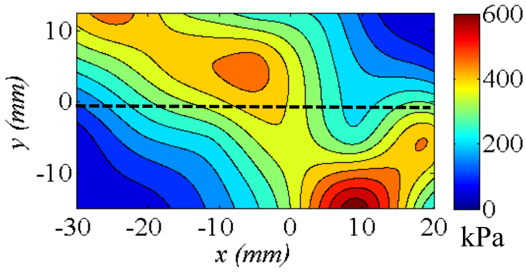

(f) δ=6 mm (back plane)

Figure 12 Stress contours drawn on vertical planes for sand sample before and after shear.

The contour maps shown in Figure 12 can be illustrated by plotting a diagram of particles contacts. A collection of discs of different sizes is gathered in the closed box as shown in Figure 13. The discs sitting on the diagonal band clearly overlap with respective neighboring discs. Based on the contact model defined in Cundall and Strack [34], these pronounced overlaps demonstrate greater levels of stressing developed at the contacts and thus add up the load shared by these discs. The discs in the remaining areas show less magnitude of overlap and thus are less effective in counteracting the shear.

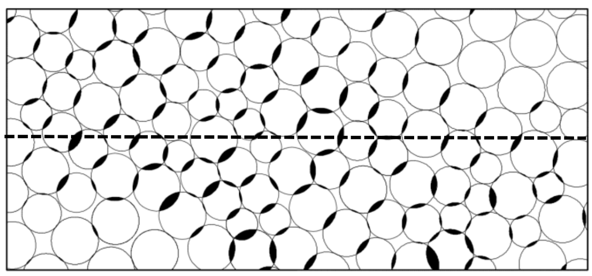

Figure 13 Schematic of discs overlapping when sheared.

Particles Displacement Vector

Particle displacement vectors are provided in Figure 14. A vector, as illustrated by the legend, has two independent properties: the magnitude and acting direction. Each of the vectors represents the displacement of a particle, with vector's start (and end) corresponding to the initial (and final) position of the particle, and the length for the travel distance. Vectors are drawn for two samples χ =0.34 and 0, respectively, both of which are sheared under σ_v=200 kPa to δ=6 mm. The two samples show similar particles displacement: significant leftward motions of particles in the lower box, and minor convex thrusts in the upper. The difference in displacement magnitude between the upper and lower boxes arises from the lower box advancing to the left which is picked up by the simulations. The convex thrusts shown in the upper box are caused due to the shear dilation [21-22, 35]. The convex thrusts are more pronounced in the rubber–sand sample (i.e. χ=0.34) than in the sand sample (i.e. χ=0) as illustrated by the vectors. Similar thrust difference was reported in Zhou et al. Zhou *et al.* [33] which concluded that large-size particles tend to generate a larger strain localization zone and result in stronger dilation. To the right of the convex thrust is a small-scale vortex zone as marked out. This is formed due to the shear strain evolution. As the shear advances, the particles in this zone undergo shear compression [36]. The particles in the vortex also fall into the less-overlap areas (Figure 13), and the loose inter-particle contacts are in favor of the particles rotations but interlocking or dilating.

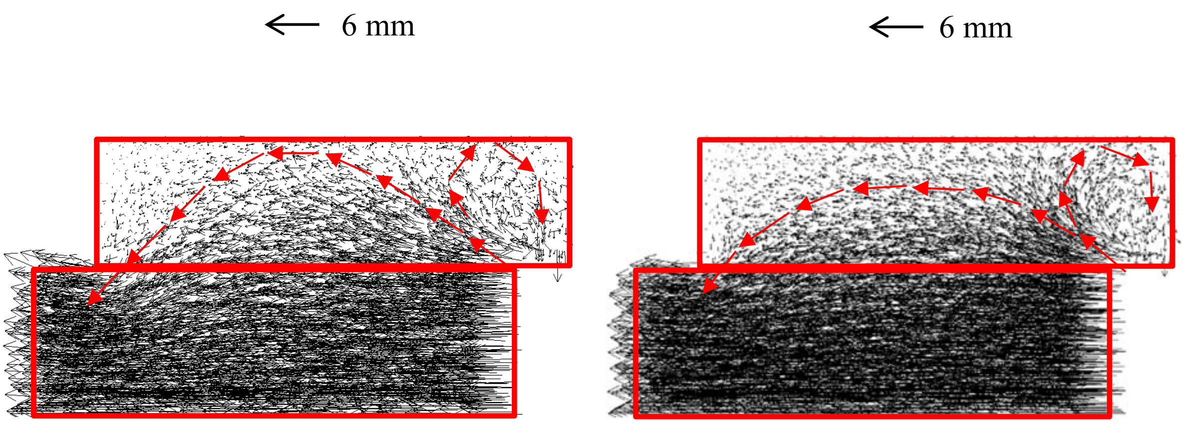

(a) χ=0.34 (b) χ=0

Figure 14 Particle displacement vectors drawn at the same scale for two samples sheared under σ_v=200 kPa to δ=6 mm.

Rubber Fraction Dependence

The above test and simulation results exhibit the rubber fraction dependence of the shear behavior. It is thus of importance to examine the dependence and develop a rubber fraction suitable for applications. The approach is to plot the shear stress vs. rubber fraction relationship for samples subjected to a set of high- to low vertical pressure σ_v. The pressure σ_v is assessed as it influences the shear stress curves. In addition to the aforementioned low- to medium pressures, two high pressures are examined: σ_v=1 and 2 MPa. The pressure values are suitable for deep (e.g., 50 to 100 m) backfilling works, e.g., mining pit renovations. The shear stress–displacement curves obtained from the developed discrete element model are presented in Figure 15. Four rubber fractions are examined, i.e. χ=0, 0.34, 0.58 and 1. It is shown that samples χ=0 and 0.34 show nearly tied curves under both pressures and the curves sit noticeably above those of samples χ=0.58 and 1. The curves difference suggests that the fraction χ=0.34 is in favor of the mixture gaining (or maintaining) shear stress; a further higher fraction may likely lead to strength decrease. This trend agrees with the strength development examined under the low- to medium pressure shear tests (Figure 4).

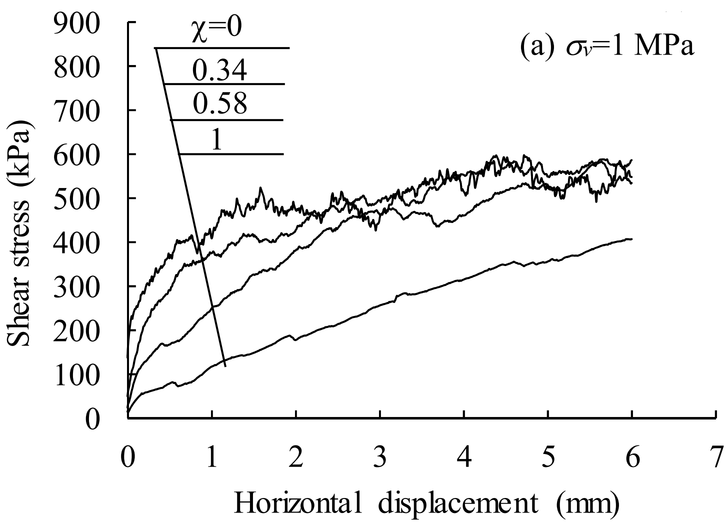

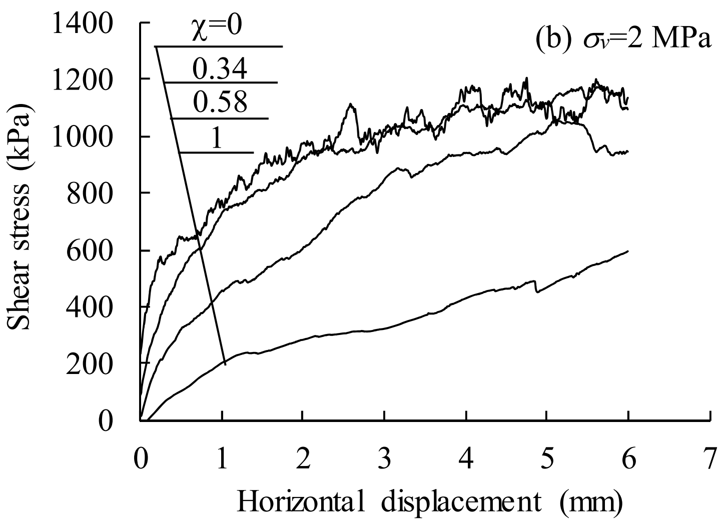

Figure 15 Shear stress–displacement curves for samples sheared under high pressures.

Define two stress points, σ_1, corresponding to the shear displacement δ=1 mm, and σ_6, to δ=6 mm, as the measures assessing the material early- and late-stage shear strength, respectively. The shear strength vs. rubber fraction relationship obtained under a set of vertical pressures is provided in Figure 16. The pressures examined include 2, 1, 0.4 and 0.1 MPa. Under the high pressures (i.e., σ_v=2 and 1 MPa), rubber fraction χ=0.34 is confirmed in favor of the shear strength development and deemed an optimal mixture. Where the vertical load reduces to 0.4 MPa or lower, the rubber inclusions exhibit marginal effect on the shear strength. That is, the rubber particles gain strength in a way similar to the sand particles where the mixtures are subjected to medium- to low loads, such as medium- to shallow-depth backfilling applications. When placed in a deep application, the mixture becomes sensitive in shear strength to the rubber content and a fraction χ=0.34 is a preferred choice to gaining shear strength.

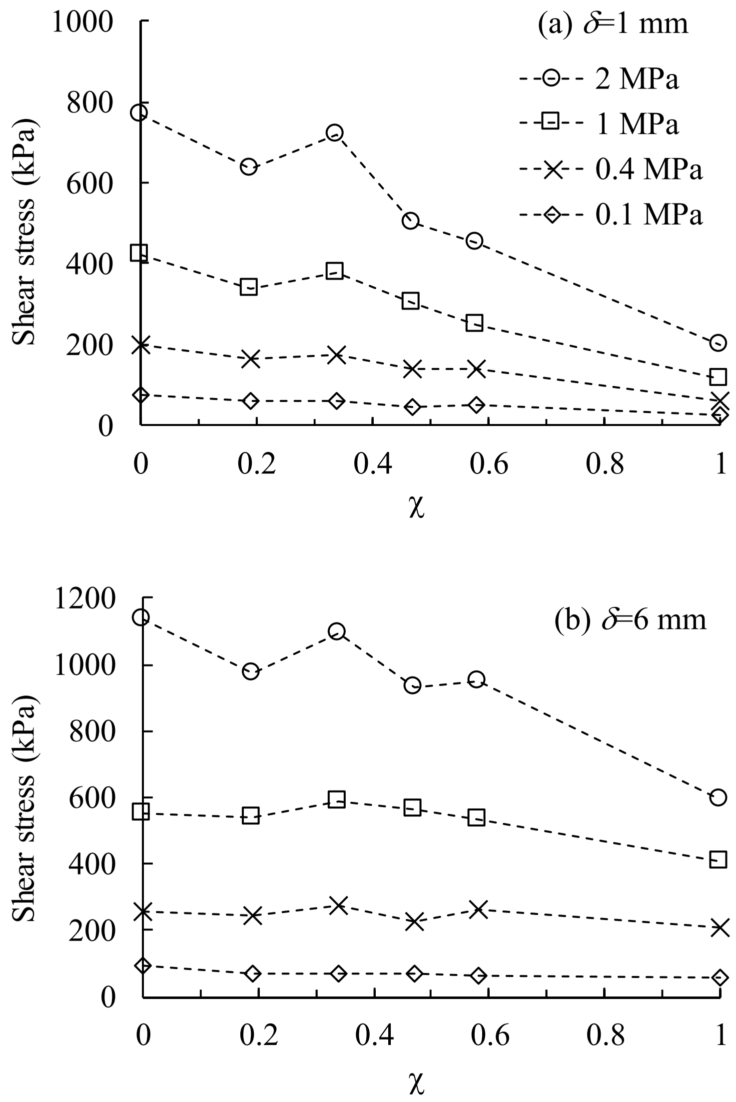

Figure 16 Shear stress obtained at two different shear distances.

Similar rubber content dependency occurs to other rubber chips or shreds based mixtures. Zornberg et al. [5] reported the optimal fraction χ=0.55 where the rubber shreds (i.e., 20–30 mm by size) were mixed with sands. Rao and Dutta [37] found that a rubber chips fraction of χ<0.35 shows strength improvement. The optimal content becomes χ=0.2–0.3 for rubber particles based mixtures [11], which agrees with the outcomes of this current study. These past and current studies suggest that the optimal rubber content is dependent on the rubber particle size, or increases with the size. When the rubber inclusions become larger, they work more like continuous media or geomemberane materials in the mixtures, enabling better particle–surface frictions. The frictions increase with the rubber contents and help mixtures gain strength. Where the rubber contents exceed respective optimal values, there are insufficient volumes of sands infilling the skeleton formed by the rubber inclusions and the packing becomes loose. In this context, the shear strength reduces.

Composite Micro-Structure

It is worth cross-checking the shear strength development (Figure 16) against the mixture packing results (Figure 6). Greater packing is obtained at χ=0.58 where the pressure acted is 0.4 MPa or less. This χ value does not agree with the optimal fraction χ=0.34 obtained for the shear strength. That is, the packing and the shear strength correspond to different optimal fractions. This finding disagrees with Ghazavi [11] associating the shear strength changes exclusively to the mixture packing. In Ghazavi [11], the maximum shear strength occurs at rubber volume fraction χ=0.2–0.3. The explanation was the occurrence of greatest packing at the same fraction, although the packing was not tested or simulated. The current study suggests that the greatest packing and maximum shear strength may not coincide at the same fraction. The packing is at χ=0.58 and the strength at χ=0.34. That means, the single strength–porosity association seems not conclusive. There are underlying factors influencing the shear strength development, one of which is the particles arrangement, in particular the large size particles (rubber) orientation.

Figure 17 illustrates three mixtures of different χ values and thus varying particles arrangement. From the left to the right, the mixtures decrease in χ values and thus bring forth varying rubber particles arrangement. An important difference among the diagrams lies in the chance of rubber particles crossing the shear plane and, if there is, the particles number. The chance and number are high where χ is high, as shown in the leftmost diagram. The particles cross the shear plane, forming a flocculated structure. Given the limited number of particle contacts on the shear plane, the force counteracting the shear is not significant. The force instead builds up where the rubber particles and the sands together sit on the shear plane, as shown in the middle diagram. The number of contacts increases, enabling better frictions and interlocking. Given the rubber particles crossing the plane, an additional component of shear resistance is gained. Where subjected to high pressures, the rubber particles help gain further resistance through the contact flattening mechanism [8]. These strength-gaining effects fade off and the shear resistance decreases if few rubber particles rest across the plane (i.e., the rightmost diagram), whereupon the sands but the rubber particles counteract the shear. Albeit the sand-contact number is significant, a portion of the on-the-plane sand finds room to relocate as illustrated (due to the rubber particles deforming) and fails to gain major shear strength from interlocking or dilating [10-11]. Given these understandings, the mixture particles arrangement is identified as an important factor influencing the shear strength development.

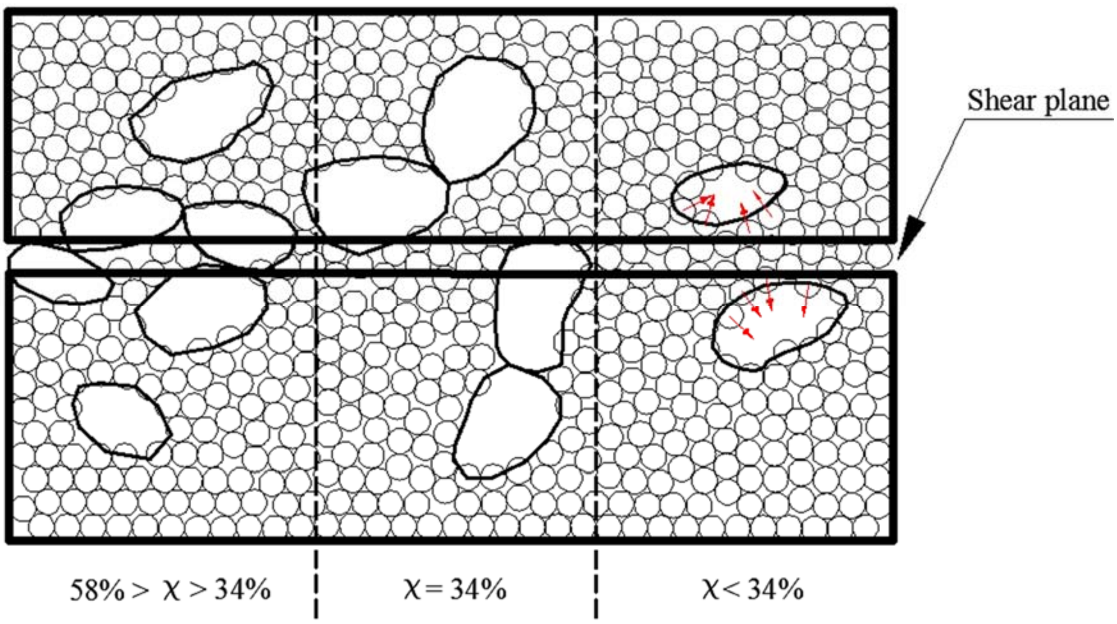

Figure 17 Schematic of mixtures arrangement as a function of rubber content.

The above three particle arrangement models can be proven based on the rubber particles sitting on the shear plane. Count the number of rubber–rubber contacts, N_c, and rubber particles, N_r. The N_c/N_r value suggests how the rubber particles orient and to what extent. Plot the N_c/N_r vs. the rubber fraction χ, as shown in Figure 18. Three representative vertical loads are examined: σ_v = 100, 1000 and 2000 kPa. Despite the varying loads, $N_c/N_r \cong 1$ where $\chi \cong 0.34$. Otherwise, N_c/N_r moves away from the unity. Where N_c/N_r=1, the particles tend to close up. This is illustrated in Figure 19. Five diagrams (*a*–*e*) are plotted, each with different particle numbers or orientations. Diagrams *b*–*c* align linearly, and Diagrams *d*–*e* close up. The orientation patterns influence the contacts number. For example, Diagram *c* has 2 contacts; Diagram *d* has 3, although the particle numbers remain the same which is 3. Determine N_c/N_r values for the five scenarios. It is suggested that the N_c/N_r value is less than 1 if particles align linearly, e.g., Diagrams *a*–*c*; and equal to or near 1 if closed up, e.g., Diagrams *d*–*e*.

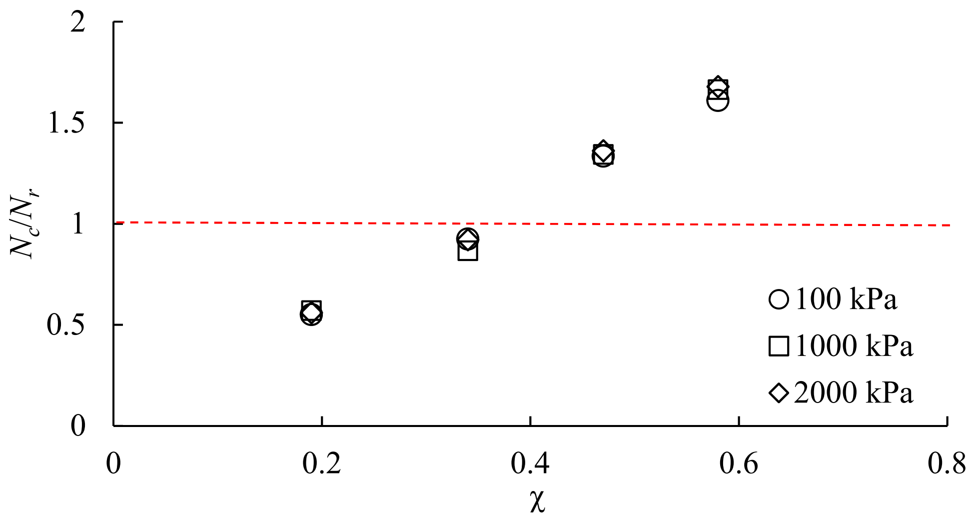

Figure 18 Rubber–rubber contacts to rubber particles vs. rubber content obtained under varying vertical loads.

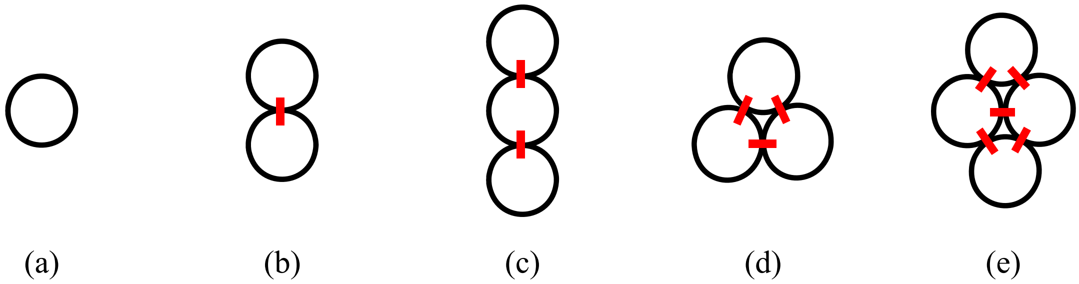

Figure 19 Particles orientation diagrams.

Figure 19's results can be applied to the direct shear simulation results. Examine the rubber particle sitting on the shear plane. The rubber particles are illustrated in Figure 20. Where χ is small, e.g. Figure 20(a) and (b), the rubber particles align linearly or are chained. Where χ increases, as of Figure 20(c) and (d), the rubber particles close up, forming a mesh. The χ-dependent rubber particles arrangement is in support of the conceptual drawings shown in Figure 17. Specifically, where χ=0.34, the rubber particles evolve a closed-up arrangement, providing room to accommodate sands. As sands and rubber particles are in balanced and well-contacted arrangements, sand–sand, sand–rubber and rubber–rubber interlocks grow; the shear strength builds up accordingly.

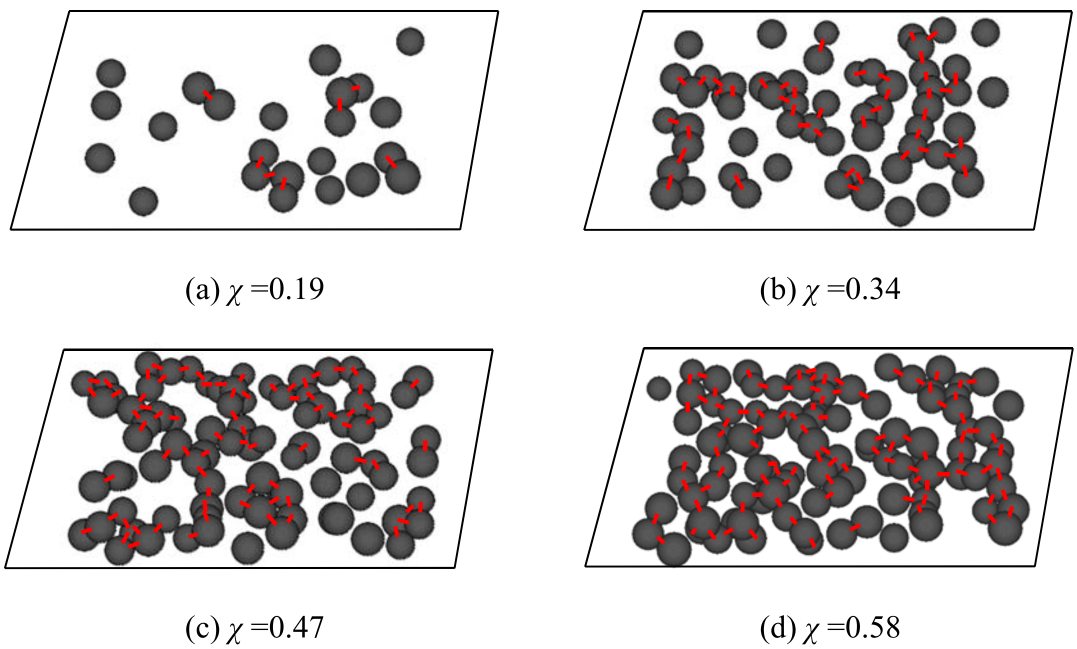

Figure 20 On-shear-plane rubble particles in samples at varying rubber contents.

Particles Rotation

Particles rotate when sheared, and the rotations are crucial to material shear behavior [38]. The rotation is assessed by examining the angular velocity of the particles of interest. As the assembly of particles exhibit varying angular velocity values, it helps the assessment if there is a solution to normalizing the values and mapping out the values for the particles of interest. Figure 21 shows the normalized values and mapping results for two samples χ=0.34 and 0, both of which are sheared under σ_v=200 kPa to δ=6 mm. Both samples exhibit a normal distribution of angular velocity, suggesting equal portions of clockwise and anti-clockwise rotations. The distributions also suggest that particles rotate at varying speed. The majority is at rest or rotates at a slow speed; a small portion (i.e., the tails) rotates faster. The particles falling into the 10% percentile as shaded are mapped out in Figure 21(a) for sample χ=0.34 and Figure 21(b) for sample χ=0, respectively. As reported in Zhang and Thornton [20], these fast-rotation particles largely sit on the diagonal band of top−right to bottom−left, conjugated with the force chains bands (Figure 9). The study [20] however does not provide details explaining the conjugation. The conjugation occurs partially due to the mechanism of inter-particle shear (i.e. the Coulomb's law of shear strength) which is illustrated in Figure 22. Two discs contact each other and, at the contact, are subjected to the normal pressure σ. The discs opt for relative displacement due to the shear force τ acting at the contact, which is expressed as:

$$\tau = \sigma \tan \phi + c \tag{4}$$

where ϕ and c are the inter-particle constants. On the top−right to bottom−left diagonal band (Figure 9), the particles are subjected to less normal pressures and, based on Eq. 4, less shear forces to rotate. That means the threshold to rotating is low, whereby the particles tend to spin faster if subjected to a driving force. The opposite occurs to the particles sitting on the top–left to bottom–right diagonal band where high-pressure contacts occur.

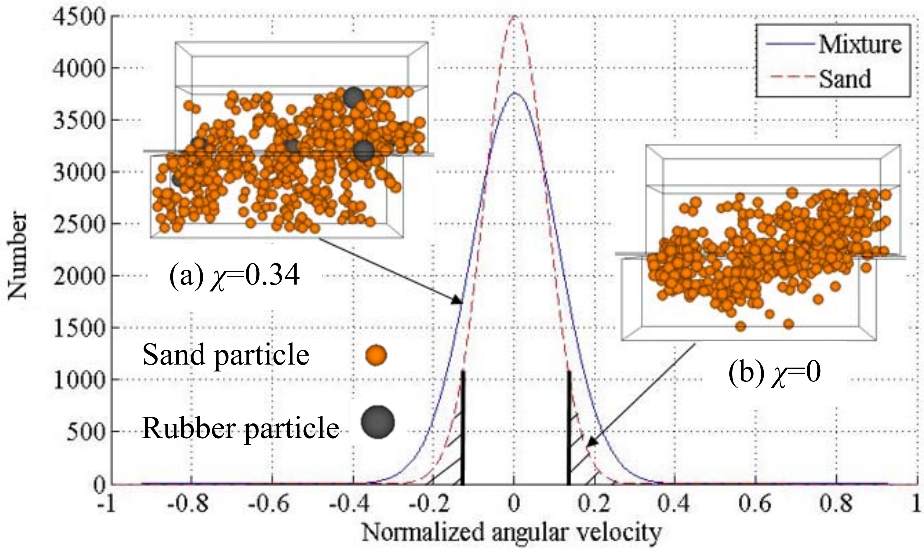

Figure 21 Particles angular velocity distribution and fast-spin particles mapping.

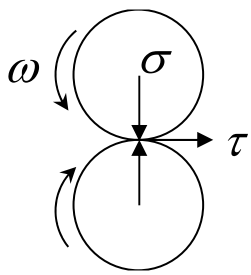

Figure 22 Inter-particle shear and rotation.

Particles Relocation

The particles relocation is examined by tracking particles motion occurred at five points: *A* to *E*, as shown in Figure 23. All of the five points originate from sample χ=0.34 being sheared under σ_v=200 kPa. The five points sit on critical places: points *A* to *C* on the shear plane separately, and points *D* and *E* in the upper and lower boxes, respectively. An accurate positioning is attained by defining the points in a 3D coordinate system (x, y, z) as illustrated. Develop the coordinate system inside the shear boxes and set the origin over the inside center.

The points A to E are positioned, through a target particle, to coordinate $(x, y, z) = (-20, 0, 0)$, $(0, 0, 0)$, $(20, 0, 0)$, $(-20, 0, 10)$ and $(20, 0, -10)$ mm, respectively. Then, around the target particle, search all neighboring particles. That is, each of the five points encompasses one target particle and its neighboring particles. The neighboring particles count from 2 to 9 depending on the point of interest. The target particles are marked out in the simulation as Nos. 2901, 3481, 3239, 3162 and 10195, respectively. Similar identity marking is provided on the neighboring particles, enabling a complete track of particles. Each of the five points comes with a pair of diagrams illustrating the particles arrangement at shear displacement δ=1 and 6 mm, respectively. It is shown that the particles on the shear plane (i.e., points A, B and C) relocate more clearly than the particles inside the boxes (i.e., points D and E) do. For instance, at point A, particle 10249 clearly moves to the left when the shear travels from 1 mm to 6 mm; in the meantime, particle 2823 joins up the target particle and particle 3097 detaches from it. Similar changes occur to points B and C. At point D (and E), however, the particles assembly remain similar in number and arrangement when the shear advances. Although the particles on the shear plane relocate noticeably, it is not clear to confirm a relocation law—either the front relocates more than the rear, or vice versa. However, the particles relocation pattern on the shear plane helps shed light on the process of shear dilation. At point A, particle 2823 pushes up particle 2507 and gradually takes over the new position. Similar replacement occurs at point C where particle 1186 moves leftward and squeezes into the position of particle 2061; particle 2061 relocates upward.

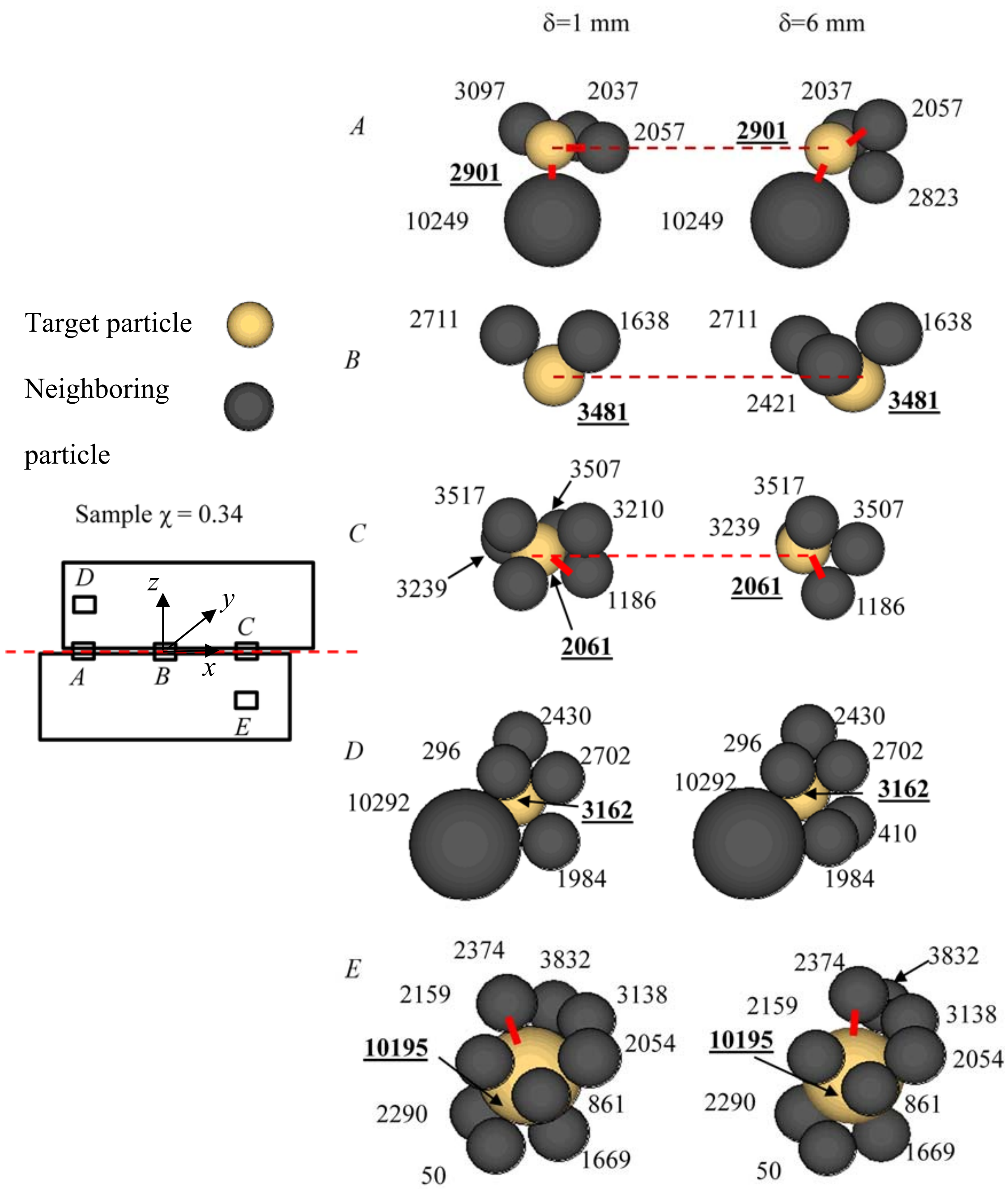

Figure 23 Particles relocations on shear plane and inside shear boxes.

CONCLUSIONS

Three-dimensional discrete element simulations on the direct shear of the rubber–sand mixtures are presented. The discrete element method enables assessing mixtures shear behavior at a particulate scale. The simulations account for the mixtures fraction, particle stiffness, grading characteristics and normal pressure changes. The simulation results include the mixture packing characteristics, shear stress–displacement relationship, particles contact force chain and force contour maps, particles displacement vector and rotations. The following conclusions are drawn.

A rubber volume fraction of χ=0.55 to 0.65 offers greater packing for the mixtures examined in this study. The greater packing enables the rubber particles sharing greater contact force. The improved packing promotes the material strain-hardening characteristics and shear ductility. A rubber volume fraction of χ=0.34 yields greater shear strength when sheared under 1 to 2 MPa pressures. Where sheared under lower pressures, the rubber-fraction dependence of shear strength is not significant. The contact forces orient diagonally. The force orientation becomes pronounced with the shear advance. Rubber particles inclusion is able to harmonize in magnitude the force band by reducing particle contacts and stiffness. The particles rotate in varying speed and the speed values follow a normal distribution. The fast-spin particles line up diagonally and in conjugation with the force chains. The particles on the shear plane relocate more noticeably than the particles away from the plane. On the plane, the particle relocations are largely consistent.

ACKNOWLEDGEMENT

This research was funded by the Australian Government through the Australian Research Council.

NOTATIONS

d	particle diameter
D_{50}	50% pass particle size
F	sum of normal force at contact
G_s	specific density of solid
k_n	normal stiffness at contact
$k_{n,1}$	normal stiffness of entity 1
$k_{n,2}$	normal stiffness of entity 2
k_s	shear stiffness at contact
$k_{s,1}$	shear stiffness of entity 1
$k_{s,2}$	shear stiffness of entity 2
N_c	number of rubber–rubber contacts on shear plane
N_r	number of rubber particles on shear plane
V	sample volume
χ	specific volume fraction
δ	shear displacement
μ	inter-particle friction coefficient
μ_1	surface friction of entity 1
μ_2	surface friction of entity 2
σ_m	mean stress at contact

σ_v vertical or normal load

ζ damping coefficient

REFERENCES

[1] Hannam P. Tyre industry divided over how to handle toxic waste. The Sydney Morning Herald. Sydney: Fairfax Media, 2014.

[2] Bosscher PJ, Edil TB, Kuraoka S. Design of highway embankments using tire chips. Journal of Geotechnical and Geoenvironmental Engineering. 1997;123(4):295-304.

[3] Lee J, Salgado R, Bernal A, Lovell C. Shredded tires and rubber-sand as lightweight backfill. Journal of Geotechnical and Geoenvironmental Engineering. 1999;125(2):132-41.

[4] Tsang H-H. Seismic isolation by rubber-soil mixtures for developing countries. Earthquake Engineering & Structural Dynamics. 2008;37(2):283-303.

[5] Zornberg JG, Cabral AR, Viratjandr C. Behaviour of tire shred sand mixtures. Can Geotech J. 2004;41(2):227-41.

[6] Anastasiadis A, Senetakis K, Pitilakis K, Gargala C, Karakasi I. Dynamic behavior of sand/rubber mixtures. Part I: Effect of rubber content and duration of confinement on small-strain shear modulus and damping ratio. Journal of ASTM International. 2012;9(2):1-19.

[7] Tsoi W, Lee K. Mechanical properties of cemented scrap rubber tyre chips. Géotechnique. 2010;61(2):133-41.

[8] Valdes JR, Evans TM. Sand-rubber mixtures: experiments and numerical simulations. Can Geotech J. 2008;45(4):588-95.

[9] Masad E, Taha R, Ho C, Papagiannakis T. Engineering properties of tire/soil mixtures as a lightweight fill material. Geotechnical Testing Journal. 1996;19(3):297-304.

[10] Ghazavi M, Sakhi MA. Influence of optimized tire shreds on shear strength parameters of sand. International Journal of Geomechanics. 2005;5(1):58-65.

[11] Ghazavi M. Shear strength characteristics of sand-mixed with granular rubber. Geotechnical & Geological Engineering. 2004;22(3):401-16.

[12] Lee C, Shin H, Lee JS. Behavior of sand–rubber particle mixtures: experimental observations and numerical simulations. International Journal for Numerical and Analytical Methods in Geomechanics. 2014;38(16):1651-63.

[13] Foose GJ, Benson CH, Bosscher PJ. Sand reinforced with shredded waste tires. Journal of Geotechnical Engineering. 1996;122(9):760-7.

[14] Balunaini U, Yoon S, Prezzi M, Salgado R. Pullout response of uniaxial geogrid in tire shred–sand mixtures. Geotechnical and Geological Engineering. 2014;32(2):505-23.

[15] Edil T, Bosscher P. Engineering properties of tire chips and soil mixtures. Geotechnical Testing Journal. 1994;17(4):453-64.

[16] Yoon S, Prezzi M, Siddiki NZ, Kim B. Construction of a test embankment using a sand–tire shred mixture as fill material. Waste Management. 2006;26(9):1033-44.

[17] Youwai S, Bergado DT. Numerical analysis of reinforced wall using rubber tire chips–sand mixtures as backfill material. Computers and Geotechnics. 2004;31(2):103-14.

[18] Patil U, Valdes JR, Evans TM. Swell mitigation with granulated tire rubber. Journal of Materials in Civil Engineering. 2010;23(5):721-7.

[19] Evans TM, Valdes JR. The microstructure of particulate mixtures in one-dimensional compression: numerical studies. Granular Matter. 2011;13(5):657-69.

[20] Zhang L, Thornton C. A numerical examination of the direct shear test. Géotechnique. 2007;57(4):343-54.

[21] Liu S, Sun D, Matsuoka H. On the interface friction in direct shear test. Computers and Geotechnics. 2005;32(5):317-25.

[22] Liu S. Simulating a direct shear box test by DEM. Can Geotech J. 2006;43(2):155-68.

[23] Kim H-K, Santamarina J. Sand–rubber mixtures (large rubber chips). Can Geotech J. 2008;45(10):1457-66.

[24] Feng K, Montoya B, Evans T. Discrete element method simulations of bio-cemented sands. Computers and Geotechnics. 2017;85(May):139-50.

[25] Itasca. PFC3D 4.0 User Manual. Minneapolis, MN USA 2008.

[26] Nakata A, Hyde M, Hyodo H, Murata. A probabilistic approach to sand particle crushing in the triaxial test. Géotechnique. 1999;49(5):567-83.

[27] Potyondy D, Cundall P. A bonded-particle model for rock. Int J Rock Mech Min Sci. 2004;41(8):1329-64.

[28] Wang Y-H, Leung S-C. A particulate-scale investigation of cemented sand behavior. Can Geotech J. 2008;45(1):29-44.

[29] De Bono JP, McDowell GR, Wanatowski D. Discrete element modelling of a flexible membrane for triaxial testing of granular material at high pressures. Geotech Lett. 2012;2(4):199-203.

[30] Coetzee C, Els D. Calibration of granular material parameters for DEM modelling and numerical verification by blade–granular material interaction. Journal of Terramechanics. 2009;46(1):15-26.

[31] Mota M, Teixeira J, Bowen WR, Yelshin A. Binary spherical particle mixed beds: porosity and permeability relationship measurement. Transactions of the Filtration Society. 2001;1(4):101-6.

[32] Wang J, Dove J, Gutierrez M. Discrete-continuum analysis of shear banding in the direct shear test. Géotechnique. 2007;57(6):513-26.

[33] Zhou Q, Shen HH, Helenbrook BT, Zhang H. Scale dependence of direct shear tests. Chinese Science Bulletin. 2009;54(23):4337-48.

[34] Cundall PA, Strack OD. A discrete numerical model for granular assemblies. Géotechnique. 1979;29(1):47-65.

[35] Masson S, Martinez J. Micromechanical analysis of the shear behavior of a granular material. Journal of Engineering Mechanics. 2001;127(10):1007-16.

[36] Indraratna B, Ngo NT, Rujikiatkamjorn C, Vinod J. Behavior of fresh and fouled railway ballast subjected to direct shear testing: Discrete element simulation. International Journal of Geomechanics. 2012;14(1):34-44.

[37] Rao GV, Dutta R. Compressibility and strength behaviour of sand–tyre chip mixtures. Geotechnical and Geological Engineering. 2006;24(3):711-24.

[38] Cui L, O'sullivan C. Exploring the macro-and micro-scale response of an idealised granular material in the direct shear apparatus. Géotechnique. 2006;56(7):455-68.